JOURNAL OF COMPUTATIONAL PHYSICS **125,** 59–70 (1996)
ARTICLE NO. 0079

A Control Volume Finite Element Numerical Simulation of the Drying of Spruce

W. J. FERGUSON AND I. W. TURNER

School of Mathematics, Queensland University of Technology, Gardens Point Campus, GPO Box 2434, Brisbane, Q4001, Australia

Received February 15, 1994; revised May 11, 1995

Drying is a process which involves heat and mass transfer both inside the porous material, where a phase change in moisture occurs from the liquid to the gaseous state, and in the external boundary layer of the convected hot dry air, which heats the porous medium. The equations which govern this process consist of three tightly coupled, highly non-linear partial differential equations for the unknown system variables of moisture content, temperature, and pressure. Due to the inherently complex boundary conditions and intricate physical geometries in any practical drying problem, an analytical solution is not possible. In order to obtain a transient drying solution it is necessary to resort to a numerical technique. Earlier researchers in this field have employed finite difference, finite element, and cell-centered control volume computational models to obtain a numerical solution to this complex problem. This paper presents a novel application of the hybrid *control volume finite element* scheme, which will lay the foundations for the solution of a timber drying problem on a deforming mesh. In order to test the performance of the simulation code over a range of differing drying conditions, numerical solutions to two timber drying problems are presented in this paper: first, a low temperature drying case with a dry bulb temperature of 80°C, and, second, for a case where the dry bulb temperature is above the boiling point of water at 120°C.

1. INTRODUCTION

Drying is a highly energy intensive industrial process which consumes between 7–15% of the total industrial energy consumption in developed countries. The annual worldwide consumption of timber is estimated to be a 1,400,000,000 m^3 [1] and the short term trend is for a significant increase. There is clearly scope for research into innovative timber drying techniques which minimise total drying times, thereby increasing the throughput of the kiln and reducing the overall energy requirements of the drying process. These industry goals can be achieved by experimental means; however, this is an expensive and time consuming endeavour. Mathematical modelling is gaining an increasing acceptance within the timber drying industry and the use of mathematical simulators, which describe the complex heat and mass transfer phenomena at a fundamental level, can provide important information which could be used in both the design and optimisation of the kiln.

Comini and Lewis [2] and Thomas *et al.* [3] were amongst the first to develop a numerical model applied to timber drying. The model incorporates the Luikov [4, 5] system of partial differential equations for a general capillary porous body for the field variables of moisture content and temperature. The pressure was assumed constant throughout the domain of interest and moisture transfer under the influence of a pressure gradient was assumed to be negligible. For high temperature drying problems, Ferguson [6] showed that the pressure term induced a significant mass transfer. The computational solution technique which was utilised to solve the governing equations was the finite element method. Dahlblom *et al.* [7] and Felix and Morlier [8] independently developed Whitaker [9] style drying models for timber which employed the finite element method as the numerical solution technique.

Michel *et al.* [10], Moyne and Perre [11, 12], Perre [13], and Turner [14] developed timber drying models based on an averaging volume, proposed by Whitaker [9], across which material parameters could be measured. The common element in these numerical models was the cell-centred control volume numerical solution scheme [15]. The control volume method has the advantage over the finite element method in that the scheme is conservative across each individual cell which is a desirable feature in any numerical drying simulation.

The motivation behind this research is to develop a computational model of the drying of timber which incorporates the effects of drying induced stresses. During drying the timber deforms due to a change in the bound water and internal stresses develop which can cause checking to occur. To be able to model accurately this behaviour, a numerical scheme must be employed which can utilise an unstructured computational mesh that deforms with the timber as the drying simulation proceeds. The cell-centred control volume method requires that the line joining two neighbouring cells is normal to the common face and this constraint inhibits the use of generalised mesh generation packages. Clearly, this method must be used with caution when applying it to non-rectangular domains. Conversely, the finite element method can discretise irregular domains

0021-9991/96 $18.00

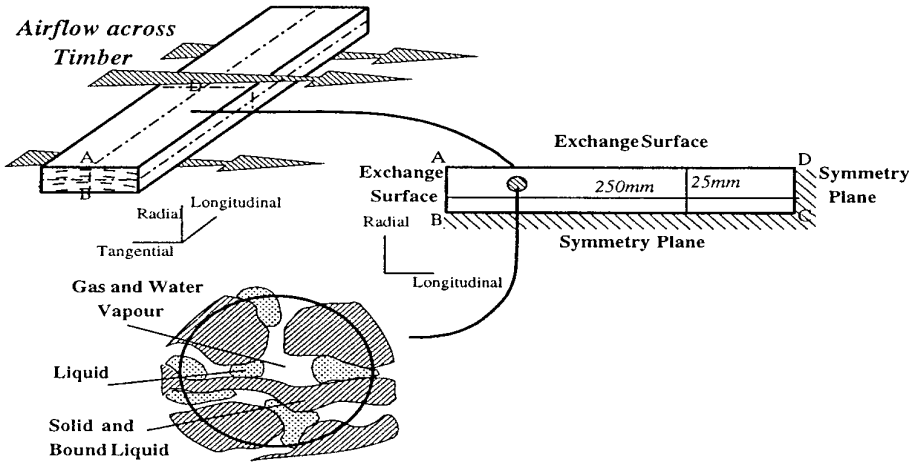

FIG. 1. Description of the wood drying process.

without any mesh constraints; however, the authors [16] have demonstrated that the control volume technique is computationally more efficient for timber drying problems.

In this research the vertex-centred control volume, otherwise known as the *control volume finite element* method (CVFE) is considered [17–20]. This particular numerical discretisation procedure is a hybrid of both the finite element method and the cell-centred control volume scheme and offers the advantages of both. The numerical technique enables a structured or unstructured grid to be used on a regular or irregular domain without alteration to the discretisation procedure. This work focusses on the application of the CVFE method to the equations which govern the drying process. To the authors' knowledge, this is the first time that this method has been applied to such a complex system of non-linear coupled partial differential equations. Furthermore, the success of the CVFE method to this particular problem will lay the foundation for the inclusion of a drying stress model, thus enabling the deforming timber to be modelled accurately.

This paper presents the control volume finite element discretisation of the governing system of partial differential equations for timber drying employing a triangular background mesh. Results from two drying simulations for spruce are presented: first, at a dry bulb temperature below the boiling point of water; second, above the boiling point. Future work includes incorporating bilinear shape functions into the model which will enable higher ordered control volumes to be used in the computational mesh.

2. MATHEMATICAL MODEL

This work consists of the theoretical study of the heat and mass transfer which occurs during the drying of a sample of wood placed in a small scale industrial kiln, Fig. 1. The transverse and longitudinal directions of the timber are considered in both the analysis and the construction of the mathematical model. For wood the relevant anisotropic material properties are known to be in mutually perpendicular directions of the longitudinal, (y), and the transverse axes, (x), therefore, an orthotropic mathematical description is sufficient.

In order to develop the mathematical model a continuum approach is adopted and the physics associated with a small averaging volume of the wood is considered (Turner [14]). Within each individual macroscopic averaging volume, shown as the cross-sectional area contained within the circle in Fig. 1, there is a solid phase (assumed to be rigid and consisting of the wood cell structure together with hygroscopically held bound liquid), a free liquid phase (water) and a gas phase (a mixture of air and water vapour). This averaging volume will be associated with every point in space and any shape may be chosen to represent it, provided the dimensions and orientations are invariant. In general the averaging volume is selected so that important model parameters, which include porosity and density, are measurable across that volume. The assumptions used in the mathematical formulation are summarised as follows:

- The solid and gas phases are continuous as is the liquid phase above the fibre saturation point.
- The binary gas mixture of air and vapour behaves like an ideal gas.
- Darcy's law holds for the gas and free liquid phases.
- Bound liquid is treated as being hygroscopically held within the solid phase.
- For moisture content above the fibre saturation point the water vapour pressure varies according to the saturated vapour pressure.
- For moisture content below the fibre saturation point, the relative humidity is defined according to the sorption isotherm data available for the particular species of wood under analysis.

• The phase kinetic energies, the fluid viscous dissipation and the work done by the body forces are negligible.
• The differential heat of sorption is included for the treatment of the enthalpy of bound water.
• Bound water migration is a molecular diffusion process whose flux is proportional to a gradient in the chemical potential.

The mathematical model is derived from the conservation laws for total mass, liquid, air, and total energy, which are given in Eqs. (1), (2), (3), and (4), respectively (see Turner [21]):

$$\frac{\partial}{\partial t}(\phi S_g \rho_g + \phi S_w \rho_{wf} + (1-\phi)\rho_{wb}) + \nabla \cdot (\chi_g \rho_g \mathbf{v}_g + \chi_w \rho_{wf} \mathbf{v}_{wf} + \chi_s \rho_{wb} \mathbf{v}_{wb}) = 0 \tag{1}$$

$$\frac{\partial}{\partial t}(\phi S_g \rho_{gv} + \phi S_w \rho_{wf} + (1-\phi)\rho_{wb}) + \nabla \cdot (\chi_g \rho_{gv} \mathbf{v}_{gv} + \chi_w \rho_{wf} \mathbf{v}_{wf} + \chi_s \rho_{wb} \mathbf{v}_{wb}) = 0 \tag{2}$$

$$\frac{\partial}{\partial t}(\phi S_g \rho_{ga}) + \nabla \cdot (\chi_g \rho_{ga} \mathbf{v}_{ga}) = 0 \tag{3}$$

$$\frac{\partial}{\partial t}(\phi S_g \rho_{gv} h_{gv} + \phi S_g \rho_{ga} h_{ga} + \phi S_w \rho_{wf} h_{wf} + (1-\phi)\rho_{wb}\bar{h}_{wb} + (1-\phi)\rho_s h_s - \phi S_g P_g) + \nabla \cdot (\chi_g \rho_{gv} \mathbf{v}_{gv} h_{gv} + \chi_g \rho_{ga} \mathbf{v}_{ga} h_{ga} + \chi_w \rho_{wf} \mathbf{v}_{wf} h_{wf} + \chi_s \rho_{wb} \mathbf{v}_{wb} h_{wb}) = \nabla \cdot (K_{\text{eff}} \nabla T) + \Phi. \tag{4}$$

It should be noted that in order to write Eq. (4) in terms of enthalpy alone, the assumption that the vapour and air phases of the gas behave in an ideal manner was used and since the solid and liquid phases are incompressible, the difference between their internal energies and their enthalpies is assumed to be negligible, i.e., $C_v \simeq C_p$. The terms $\bar{h}_{wb}$ and h_{wb} are defined as the averaged and specific enthalpies of the bound liquid. The flux expressions for the gas, free liquid, bound liquid, vapour, and air phases are

$$\chi_g \rho_g v_g = \frac{-\mathbf{K}_{go}\mathbf{K}_g M P_g}{RT\mu_g}\left(\nabla P_g - \frac{MP_g g}{RT}\right) \tag{5}$$

$$\chi_w \rho_{wf} \mathbf{v}_{wf} = \frac{-\mathbf{K}_{wo}\mathbf{K}_w \rho_w}{\mu_w}(\nabla(P_g - P_c) - \rho_w g) \tag{6}$$

$$\chi_s \rho_{wb} \mathbf{v}_{wb} = -(1-\phi)\mathbf{D}_b\left(\frac{\Psi}{RT}\frac{\partial \rho_{wb}}{\partial \Psi}\left(\frac{d\mu_{vo}}{dT} + R\ln\Psi + \frac{\Delta h_w}{T}\right)\nabla T + \nabla \rho_{wb}\right) \tag{7}$$

$$\chi_g \rho_{gv} \mathbf{v}_{gv} = \frac{-\mathbf{K}_{go}\mathbf{K}_g M_v P_{gv}}{RT\mu_g}\left(\nabla P_g \mathrm{g} - \frac{MP_g g}{RT}\right) - \frac{\mathbf{D}_{\text{eff}} P_g M_a M_v}{M\,RT}\nabla\left(\frac{P_{gv}}{P_g}\right) \tag{8}$$

$$\chi_g \rho_{ga} \mathbf{v}_{ga} = \chi_g \rho_g \mathbf{v}_g - \chi_g \rho_{gv} \mathbf{v}_{gv} \tag{9}$$

The quantities $\mathbf{K}_g$, $\mathbf{K}_w$, $\mathbf{D}_b$, and $\mathbf{D}_{\text{eff}}$ are second-order tensors which define the gaseous permeability, liquid permeability, bound liquid diffusivity, and effective diffusivity, respectively. For wood, which is an orthotropic medium, these tensors are diagonal.

If (5) to (9) are substituted into Eqs. 2 to 4, a system of three coupled highly non-linear partial differential equations are obtained which govern the process of timber drying:

$$A_{11}\frac{\partial X}{\partial t} + A_{12}\frac{\partial T}{\partial t} = \nabla \cdot (K_{11}\nabla X) + \nabla \cdot (K_{12}\nabla T) + \nabla \cdot (K_{13}\nabla P) \tag{10}$$

$$A_{21}\frac{\partial X}{\partial t} + A_{22}\frac{\partial T}{\partial t} + A_{23}\frac{\partial P}{\partial t} = \nabla \cdot (K_{21}\nabla X) + \nabla \cdot (K_{22}\nabla T) + \nabla \cdot (K_{23}\nabla P) \tag{11}$$

$$A_{31}\frac{\partial X}{\partial t} + A_{32}\frac{\partial T}{\partial t} + A_{33}\frac{\partial P}{\partial t} = \nabla \cdot (K_{31}\nabla X) + \nabla \cdot (K_{32}\nabla T) + \nabla \cdot (K_{33}\nabla P). \tag{12}$$

The governing system of partial differential equations is cast in this form is to emulate the appearance of the Luikov equations [4], which are well known in the field of drying. The three independent system variables are moisture content X, temperature T, and pressure P. The kinetic K_{ij} and capacity A_{ij} coefficients are explained and presented in greater detail by Turner [14]. The phenomological coefficients vary with the moisture content, temperature, and pressure within the timber; hence, these coefficients are highly non-linear. To illustrate the complexity of the system of equations and in particular to highlight the non-linear nature of the coefficients, the capacity and kinetic coefficients from the first equation, Eq. (10), are summarised,

$$A_{11} = 1 + \frac{\phi M_v (1-S_w)}{\rho_o RT}\frac{\partial P_{gv}}{\partial X_{wb}} - \frac{P_{gv} M_v}{\rho_{wf} RT} H(X - X_{fsp}) \tag{13}$$

$$A_{12} = \frac{\phi M_v (1-S_w)}{\rho_o RT^2}\left(T\frac{\partial P_{gv}}{\partial T} - P_{gv}\right) \tag{14}$$

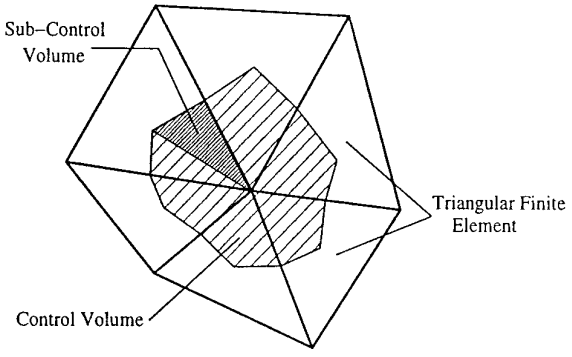

FIG. 2. Construction of a control volume from the triangular finite element mesh.

$$K_{11} = -\frac{\rho_{wf} K_{wo} K_w}{\rho_o \mu_w} \frac{\partial P_c}{\partial X_{wf}} H(X - X_{fsp}) + D_b(1 - H(X - X_{fsp})) + \frac{D_{\text{eff}} M_a M_v}{\rho_o M RT} \frac{\partial P_{gv}}{\partial X_{wb}} \quad (15)$$

$$K_{12} = -\frac{\rho_{wf} K_{wo} K_w}{\rho_o \mu_w} \frac{\partial P_c}{\partial T} H(X - X_{fsp}) + \frac{D_{\text{eff}} M_a M_v}{\rho_o M RT} \frac{\partial P_{gv}}{\partial T} + D_b \left(\frac{\Psi}{RT} \frac{\partial X_w}{\partial \Psi} \left(\frac{d\mu_{vo}}{dT} + R \ln \Psi + \frac{\Delta h_w}{T} \right) \right) (1 - H(X - X_{fsp})) \quad (16)$$

$$K_{13} = \frac{\rho_{wf} K_{wo} K_w}{\rho_o \mu_w} + \frac{K_{go} K_g M_v P_{gv}}{\rho_o RT \mu_g} - \frac{D_{\text{eff}} M_a M_v P_{gv}}{\rho_o M RT P_g}, \quad (17)$$

where $H(x)$ represents the Heaviside function.

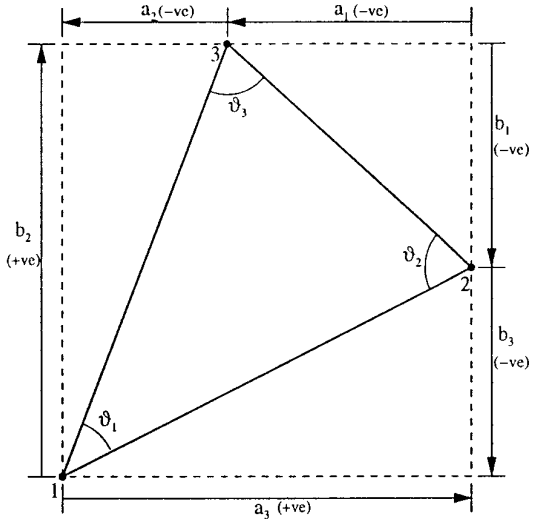

FIG. 3. Definition of geometric factors in a finite element.

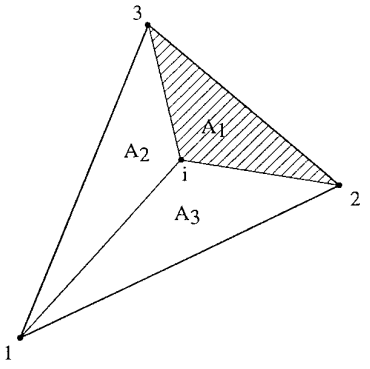

FIG. 4. Definition of area coordinates for a linear triangular element.

3. BOUNDARY CONDITIONS

For the configuration shown in Fig. 1, two types of boundary conditions exist. Across the symmetry planes (faces BC and CD) an adiabatic boundary condition is imposed, the gradients of temperature, moisture content, and pressure normal to the surfaces are assumed to be zero; i.e., no flow occurs across these surfaces. For the exchange surfaces (faces AB and AD), across which heat is supplied and moisture evaporates into the airstream, it is assumed that the driving forces across these boundaries are of the form proposed by Perre and Degiovanni [22]:

$$F_{\text{mass}} = k_m c M_v \frac{2.2}{2.2 - x_v - x_{v0}} (x_v - x_{v0}) \quad (18)$$

$$F_{\text{heat}} = Q(T - T_0), \quad (19)$$

where x_v and T are the molar fraction of the gas vapour and temperature at the surface, respectively, and x_{vo} and T_o are the molar fraction of the gas vapour and temperature characteristic of the external drying conditions. The quantities k_m and Q are the mass transfer and heat transfer coefficients, respectively. A Dirichlet boundary condition is imposed upon the pressure term along the exchange surfaces and is fixed at atmospheric pressure (101325 Pa). In summary the boundary conditions at the exchange surfaces are given as

$$(\chi_g \rho_{gv} \mathbf{v}_{gv} + \chi_w \rho_{wf} \mathbf{v}_{wf} + \chi_s \rho_{wb} \mathbf{v}_{wb}) \cdot \mathbf{n} = F_{\text{mass}} \quad (20)$$

$$(\chi_g \rho_{gv} \mathbf{v}_{gv} h_{gv}) + \chi_g \rho_{ga} \mathbf{v}_{ga} h_{ga} + \chi_w \rho_{wf} \mathbf{v}_{wf} h_{wf} + \chi_s \rho_{wb} \mathbf{v}_{wb} h_{wb} - \mathbf{K}_{\text{eff}} \nabla T) \cdot \mathbf{n} = F_{\text{heat}} + h_{gv} F_{\text{mass}}. \quad (21)$$

4. CONTROL VOLUME FINITE ELEMENT SOLUTION METHOD

The equations which govern the timber drying process, Eqs. (10) to (12), are a system of three tightly coupled

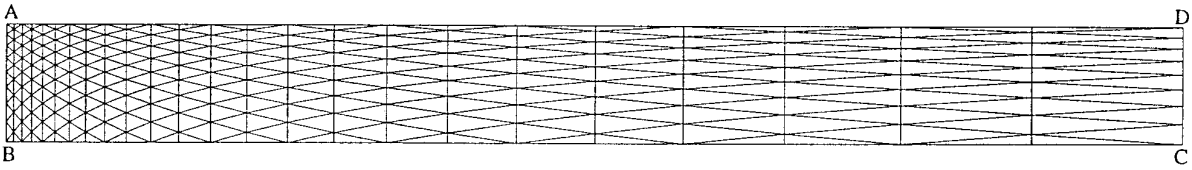

FIG. 5. Finite element linear triangular mesh.

highly non-linear partial differential equations. Analytical solutions exist for one-dimensional problems and two-dimensional problems which contain the simplest of boundary conditions and physical geometries and where the phenomological coefficients are assumed constant within the ranges of moisture content, temperature, and pressure under study. In practice, timber drying problems are comprised of intricate boundary conditions which render the governing equations unsolvable by analytic means. To overcome this drawback it is necessary to resort to a numerical solution technique. In this paper, the numerical solution technique employed to solve the system of equations, described by Eqs. (10) to (12), is the *control volume finite element* method, alternatively known as *vertex-centred control volume* method, which is a hybrid of the finite element method and the cell-centred control volume method.

To illustrate the discretisation process involved with the control volume finite element method only the governing equation for temperature, Eq. (11), will be studied. A similar procedure is followed for both the moisture content and pressure governing equations, Eqs. (10) and (12), respectively; however, they are omitted for the sake of clarity. The discretisation process is initiated by utilising the integrated form of the equation:

$$\begin{aligned}\int_{\Delta t}\int_{V} A_{21}\frac{\partial X}{\partial t} + A_{22}\frac{\partial T}{\partial t} + A_{23}\frac{\partial P}{\partial t}\,dV\,dt \\ = \int_{\Delta t}\int_{V} \nabla\cdot(K_{21}\nabla X) + \nabla\cdot(K_{22}\nabla T) \\ + \nabla\cdot(K_{23}\nabla P)\,dV\,dt.\end{aligned} \tag{22}$$

Applying the Gauss divergence theorem to the right-hand side of Eq. (22) and integrating the left-hand side gives

$$\begin{aligned}V_i\frac{(X_i^{n+1}-X_i^n)}{\Delta t}A_{21} + V_i\frac{(T_i^{n+1}-T_i^n)}{\Delta t}A_{22} \\ + V_i\frac{(P_i^{n+1}-P_i^n)}{\Delta t}A_{23} \\ = \int_s (K_{21}\nabla X\cdot\mathbf{n} + K_{22}\nabla T\cdot\mathbf{n} + K_{23}\nabla P\cdot\mathbf{n})\,ds,\end{aligned} \tag{23}$$

where V_i is the area of the control volume under consideration. The time derivative terms are discretised using a backward Euler timestepping scheme, where the superscripts n and $n+1$ represent time levels. Note that this is a fully implicit scheme and all non-linear coefficients are evaluated at the $(n+1)^{\text{th}}$ time level. The integral in Eq. (23) is a surface integral which must be approximated over all edges of the control volume; however, for the two-dimensional case, this reduces to a line integral. For the control volume finite element method, the finite element mesh can be viewed as a *background* or an *interpolation* grid. The control volume computational mesh is constructed from the finite element mesh by connecting the centroid of an individual finite element to the midpoint of each face. Therefore, each node on the finite element mesh is a representative point around which the control volume is constructed. Figure 2 demonstrates the construction of a polygonal control volume, which may, or may not be, convex.

The integral in Eq. (23) can be rewritten as

$$\begin{aligned}\int_s K_{21}\nabla X\cdot\mathbf{n} + K_{22}\nabla T\cdot\mathbf{n} + K_{23}\nabla P\cdot\mathbf{n}\,ds \\ = \int_\Gamma \left(K_{x21}\frac{\partial X}{\partial x}\Delta y - K_{y21}\frac{\partial X}{\partial y}\Delta x\right)d\Gamma \\ + \int_\Gamma \left(K_{x22}\frac{\partial T}{\partial x}\Delta y - K_{y22}\frac{\partial T}{\partial y}\Delta x\right)d\Gamma \\ + \int_\Gamma \left(K_{x23}\frac{\partial P}{\partial x}\Delta y - K_{y23}\frac{\partial P}{\partial y}\Delta x\right)d\Gamma,\end{aligned} \tag{24}$$

where Γ denotes the boundary; K_{xkl} and K_{ykl} represent the x and y components of the kinetic coefficient K_{kl}, respectively; Δx and Δy represent the x and y components of the face length; and the normal to the control volume face is represented by the vector $(\Delta y, -\Delta x)$. To evaluate the terms in Eq. (24), consider the triangular element in Fig. 3, where a_i and b_i are obtained from the anticyclic permutation of x and the cyclic permutation of y, respectively. These terms are defined in Eq. (25):

$$\begin{aligned}a_1 &= x_3 - x_2, \quad b_1 = y_2 - y_3, \\ a_2 &= x_1 - x_3, \quad b_2 = y_3 - y_1, \\ a_3 &= x_2 - x_1, \quad b_3 = y_1 - y_2.\end{aligned} \tag{25}$$

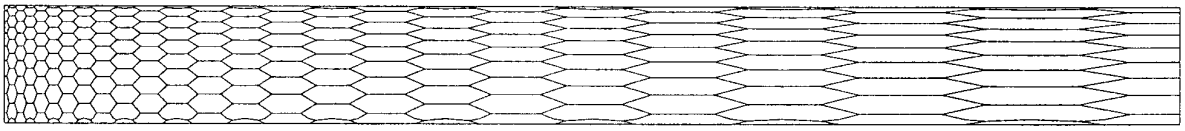

FIG. 6. Control volume polygonal mesh.

Figure 4 shows the definitions of the linear interpolation functions for a linear triangular element. The interpolation functions are also known as *shape* or *basis* functions and are explained in greater detail by Zienkiewicz [23]. The nodal shape functions, which are given in terms of area coordinates [23], for any point inside Δ_{123} are given by

$$N_i = \frac{A_i}{A}, \quad i = 1, 2, 3, \tag{26}$$

where A_i represents the areas of the triangles in the element and A is the total area of the triangular element:

$$A = \sum_{i=1}^{3} A_i. \tag{27}$$

Any variable in the element Δ_{123}, Fig. 4, may be defined if the nodal values are known. For example,

$$\Phi \simeq \sum_{i=1}^{3} N_i \Phi_i. \tag{28}$$

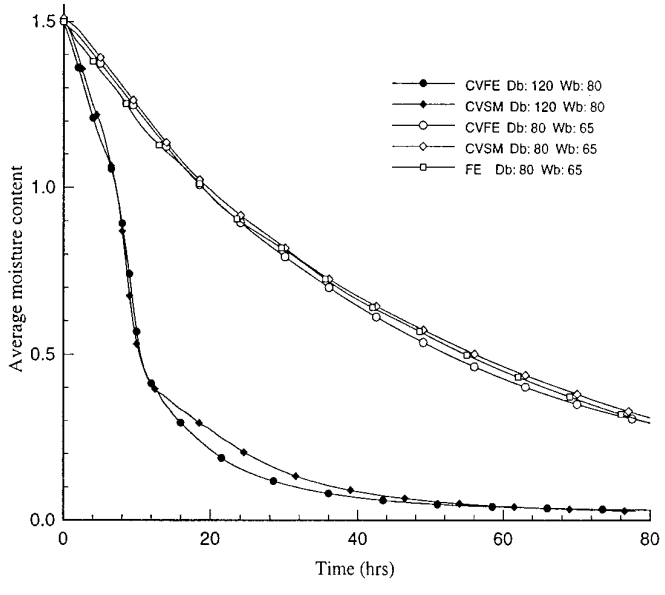

FIG. 7. Average moisture content versus time.

From simple geometry, it can be shown that the derivatives of N_i with respect to x and y are

$$\frac{\partial N_i}{\partial x} = \frac{b_i}{2A}, \quad \frac{\partial N_i}{\partial y} = \frac{a_i}{2A}. \tag{29}$$

The derivatives of any variable with respect to x and y within the element can be approximated in the same manner as the variable itself:

$$\frac{\partial \Phi}{\partial x} \simeq \sum_{i=1}^{3} \frac{\partial N_i}{\partial x} \Phi_i, \quad \frac{\partial \Phi}{\partial y} \simeq \sum_{i=1}^{3} \frac{\partial N_i}{\partial y} \Phi_i. \tag{30}$$

If Eq. (24) and the approximations to the global derivatives, Eqs. (30) are substituted into Eq. (23), the final form of the discretised equations are obtained:

$$\begin{aligned}
&\frac{V_i}{\Delta t}(X_i^{n+1} - X_i^n) A_{21}^{n+1} + \frac{V_i}{\Delta t}(T_i^{n+1} - T_i^n) A_{22}^{n+1} \\
&\quad + \frac{V_i}{\Delta t}(P_i^{n+1} - P_i^n) A_{23}^{n+1} \\
&= \sum_{j=1}^{N_{\text{scv}}} \sum_{s=1}^{N_{\text{vert}}} \left(K_{x21j}^{n+1} \frac{\partial N_{sj}}{\partial x} \Delta y_j - K_{y21j}^{n+1} \frac{\partial N_{sj}}{\partial y} \Delta x_j \right) X_s^{n+1} \\
&\quad + \sum_{j=1}^{N_{\text{scv}}} \sum_{s=1}^{N_{\text{vert}}} \left(K_{x22j}^{n+1} \frac{\partial N_{sj}}{\partial x} \Delta y_j - K_{y22j}^{n+1} \frac{\partial N_{sj}}{\partial y} \Delta x_j \right) T_s^{n+1} \\
&\quad + \sum_{j=1}^{N_{\text{scv}}} \sum_{s=1}^{N_{\text{vert}}} \left(K_{x23j}^{n+1} \frac{\partial N_{sj}}{\partial x} \Delta y_j - K_{y23j}^{n+1} \frac{\partial N_{sj}}{\partial y} \Delta x_j \right) P_s^{n+1},
\end{aligned} \tag{31}$$

where N_{vert} represents the number of vertices of the finite element; N_{scv} is the number of sub-control volumes, i.e., the number of faces in the polygonal control volume; Δx and Δy are the lengths of the components of the control volume face in the x and y directions, respectively; i represents the control volume under consideration; A_{kl} is the capacity coefficient evaluated at point i; and K_{xkl} and K_{ykl} are the kinetic coefficients which are evaluated at the midpoint of sub-control volume face j; Δt is the timestep. Fung *et al.* [19] demonstrated that the CVFE discretisation procedure, Eq. (31) produces the same discretised equation as the Petrov–Galerkin finite element method for single phase flow. When all the govern-

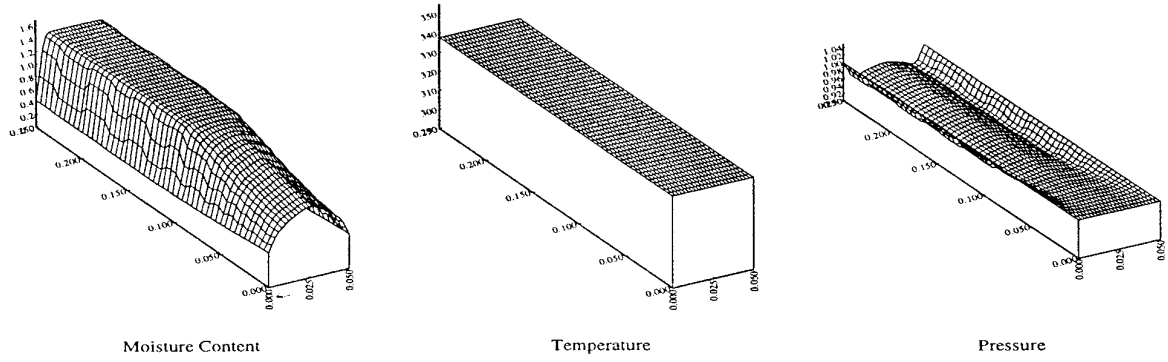

FIG. 8. Dry bulb, 80; wet bulb, 65; time, 10 h.

ing equations are taken into consideration and the discretised form is evaluated for all the control volumes contained within the computational grid, a set of non-linear equations result.

Convection of the gaseous phase becomes dominant over the diffusional terms for the high temperature drying example and the terms due to convection are evaluated with upstream weighting (Patankar [15]),

$$\begin{aligned} K_{ij} &= K_{ij}^{p}, \quad \text{if } P_g^p > P_g^q \\ K_{ij} &= K_{ij}^{q}, \quad \text{if } P_g^q > P_g^p, \end{aligned} \tag{32}$$

where p and q are the centroids of the control volume on either side of the control volume face under consideration and P_g^p and P_g^q represent the total gaseous pressure at points p and q, respectively.

The system of equations is non-linear and in order to advance the solution in time from the n^{th} to the $(n+1)^{\text{th}}$ time level a fixed point iterative scheme is employed. The numerical solution comprises two distinct phases, known as *outer iteration*, where the non-linearity is processed, and *inner iteration*, where the linearised system is solved. For the outer iterations, starting values are assumed for the system variables and the kinetic and capacity coefficients are evaluated. A linearised system of equations, Eq. (31), is constructed and solved to obtain updated values for the system variables. These updated values are then used for the next outer iteration. When the error between two consecutive outer iterations is less than a prescribed tolerance, the solution for the $(n+1)^{\text{th}}$ time level is deemed to have converged. The linearised system of equations is diagonally dominant and block symmetric and was solved using the iterative solver GMRES, with an ILU block preconditioner.

In order to ensure the convergence of the outer procedure it is often desirable to slow down the changes in the system variables from iteration to iteration. This process is known as *underrelaxation* and is shown in Eq. 33,

$$\Phi^{i+1} = \alpha\Phi^{i} + (1-\alpha)\,\Phi^{i-1}, \quad 0 \le \alpha \le 1, \tag{33}$$

where Φ represents the system variables and $i+1$, i, and $i-1$ represent the next, current, and previous iteration, respectively. Another strategy for assisting the convergence of the system is to use an adaptive time-stepping technique. During the constant rate period of

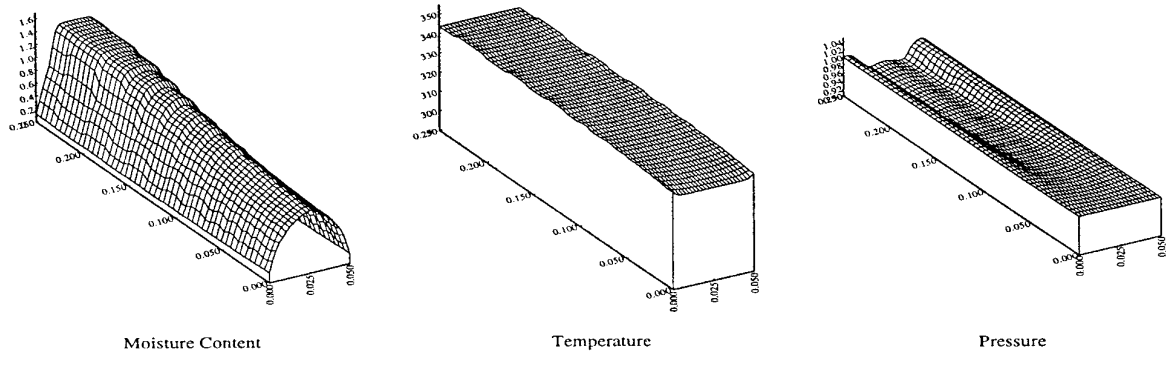

FIG. 9. Dry bulb, 80; wet bulb, 65; time, 25 h.

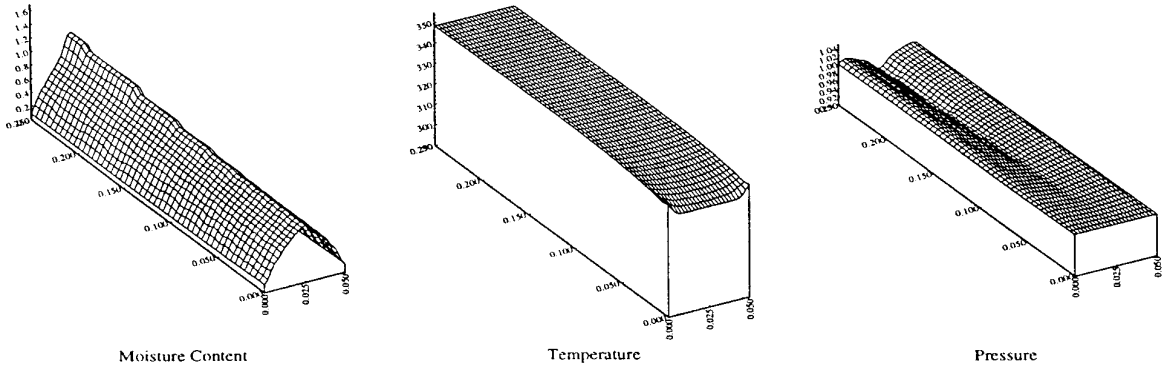

FIG. 10. Dry bulb, 80; wet bulb, 65; time, 50 h.

drying and in the final stages of the falling rate period, the distributions of moisture content, temperature, and pressure are ''well-behaved'' and a large timestep may be employed. However, in the critical stage of drying, where the moisture content passes through and goes below the fibre saturation point, a much smaller timestep is necessary. The number and quality of the iterations dictate the choice of the underrelaxation and timestep factors.

The equation which describes the mass flux, Eq. (18), is complex and highly non-linear, being a function of the system variables, moisture content, and temperature. In order to stabilise the iterative process and to increase the convergence rate, by increasing the diagonal dominance of the linear system of equations, the boundary fluxes across the exchange surfaces are linearised using a Taylor series expansion.

5. NUMERICAL SIMULATION RESULTS

The species of wood under consideration is spruce with material properties being taken directly from the literature [22]. A low temperature and a high temperature timber drying problem are presented.

Case 1. Dry bulb temperature 80°C, wet bulb temperature 65°C.

Case 2. Dry bulb temperature 120°C, wet bulb temperature 80°C.

The timber is placed in a dryer and hot air, having a uniform velocity of 2 m/s, is convected across the surface of the timber. The air stream has a mass transfer coefficient of 0.014 ms^{-1} and a heat transfer coefficient of 14 $Wm^{-2}K^{-1}$. The initial conditions throughout the spruce sample were moisture content 150%, temperature 25°C, and pressure 1 atmosphere (101325 Pa). The moisutre content within the timber is measured as kilograms of moisture per kilogram of dry solid and is known as the *dry basis* moisture content.

In reality the physical problem is three-dimensional, however, due to the similarity of the material properties in the radial and transverse directions, the problem reduces to a two-dimensional study. Figure 1 shows the drying configuration and the timber section under analysis, with the exchange surfaces across which the air is blown and

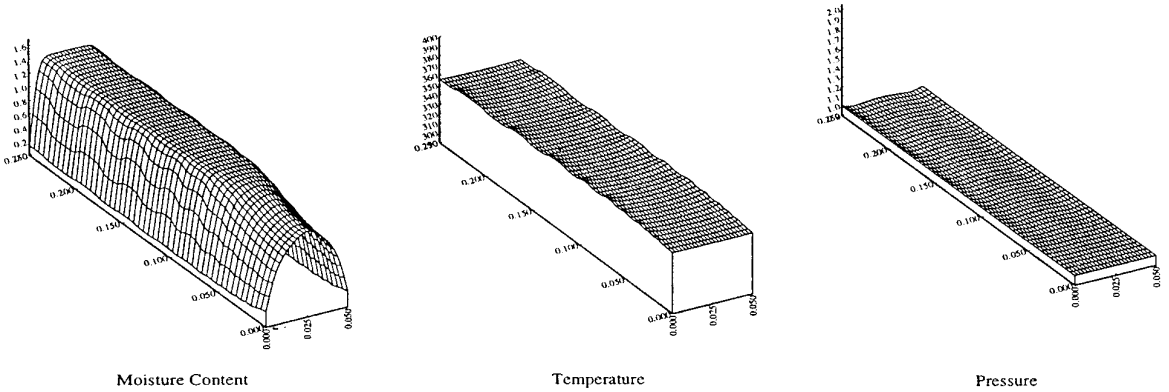

FIG. 11. Dry bulb, 120; wet bulb, 80; time, 5 h.

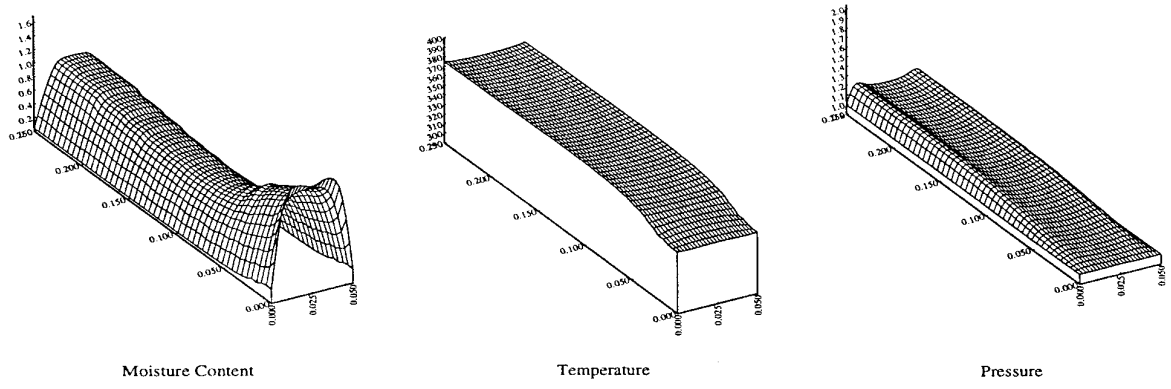

FIG. 12. Dry bulb, 120; wet bulb, 80; time, 10 h.

the symmetry planes in the longitudinal and transverse directions across which neither heat nor mass transfer takes place.

The section of timber under investigation has dimensions 50 mm × 500 mm; however, due to the planes of symmetry in the transverse and longitudinal directions only a quarter section (25 mm × 250 mm) of the timber needs be modelled. The finite element interpolation grid and the control volume computational mesh used for the analyses are shown in Figs. 5 and 6, respectively. Four hundred and eight linear triangular elements were used in the finite element mesh. The sole purpose of this grid is to enable the system variables, moisture content, temperature, and pressure, the capacity coefficients A_{ij} and the kinetic coefficients K_{ij} to be interpolated at any point within the domain of interest, according to the standard finite element area shape functions. The finite element mesh, Fig. 5, exhibits a local refinement near point A, which is where the greatest moisture content, temperature, and pressure gradients are expected to arise. The control volume mesh, Fig. 6, which is the actual computational grid, consists of 237 irregular duodecagons. This mesh is deduced from the finite element background mesh by joining the centroid of each finite element to the midpoint of each side.

The numerical results are presented across the whole of the transverse direction; i.e., the results are reflected about the axis of symmetry in the longitudinal direction, in the form of a three-dimensional surface plot, where the x and y axes represent the transverse and longitudinal directions, respectively, and the z axis represents one of the system variables (moisture content, temperature, or pressure). The graphical grid is deduced from the numerical mesh by means of linear interpolation, which may introduce small errors into the displayed results, but it is felt that this three-dimensional method of graphical representation gives a clearer understanding of the processes which are taking place within the timber sample.

Figure 7 shows the average moisture content within the timber versus time for the two drying cases presented in this paper. For case 1 (low temperature drying), the results obtained from the control volume finite element model are compared against those from a finite element (FE) and a cell-centred control volume (CVSM) model; for case 2 (high temperature drying) the results are plotted against

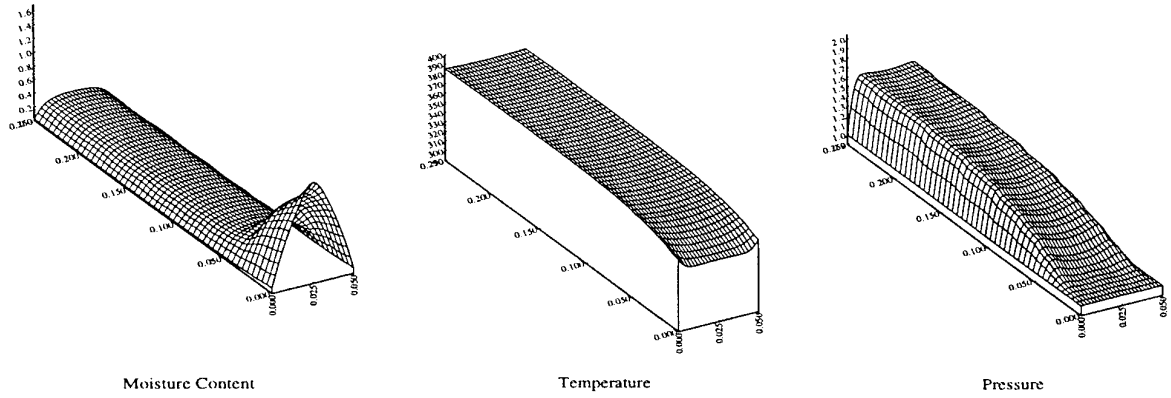

FIG. 13. Dry bulb, 120; wet bulb, 80; time, 15 h.

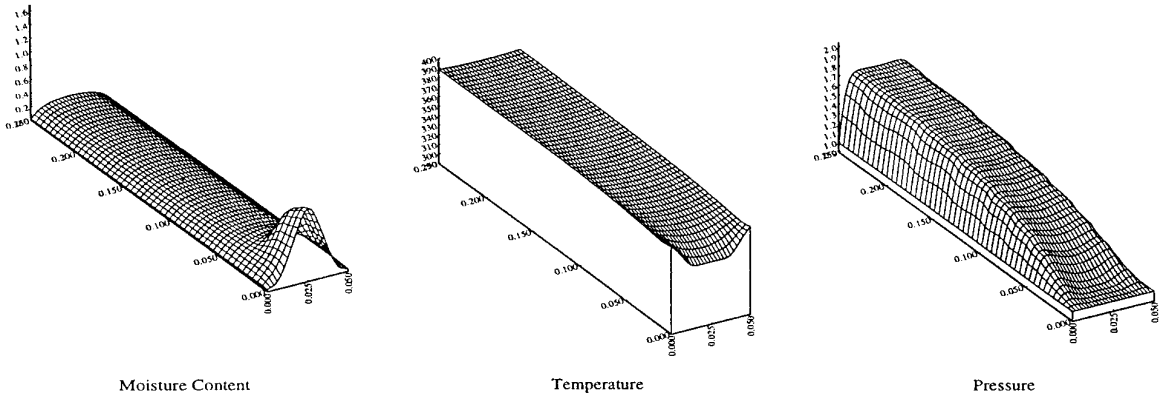

FIG. 14. Dry bulb, 120; wet bulb, 80; time, 20 h.

those obtained using the cell-centred approach. Two distinct regions are identifiable in Fig. 7: first the constant rate drying period; second the falling rate drying period. The constant rate drying period occurs up to approximately 10 h and is caused by a constant temperature gradient across the drying surfaces. Within the timber the temperature gradient is negligible, the heat supplied by the airstream is used in the change of phase of the moisture within the timber from the liquid to the gaseous state and in the evaporation at the surface. The moisture migrates from the interior of the timber to the drying surfaces due to capillarity under the influence of a moisture content gradient. As the temperature of the timber drying surfaces rises from the wet bulb to the dry bulb temperature of the airstream, the temperature gradient across the drying surfaces decreases, causing the falling rate drying period to rise.

The results presented in this paper, Figs. 7 to 15, exhibit the same characteristics as the numerical simulations which have been published by Turner [14] and Perre and Degiovanni [22], who employed the structured cell-centred control volume method, and Ferguson and Turner [16], who used the finite element method for a low temperature timber drying example. Future work includes a more detailed comparison of the numerical results obtained from the differing unstructured control volume computational techniques.

5.1. *Case* 1: *Dry bulb*, 80°C; *wet bulb*, 65°C

This low temperature drying problem concerns a timber sample in an airstream, which has a wet bulb temperature of 65°C and a dry bulb temperature of 80°C. The average moisture content versus time graph is shown in Fig. 7. The constant rate drying period extends to a time of approximately 10 h, during which time the temperature throughout the timber remains at the wet bulb temperature of the airstream. Once the surface of the timber dries, the cooling effect due to evaporation of moisture into the airstream decreases and the temperature of the timber rises to the dry bulb temperature of the airstream. After the temperature of the timber rises above the wet bulb temperature of the airstream, then the falling rate drying period begins, during which time the temperature gradient across the timber sample decreases.

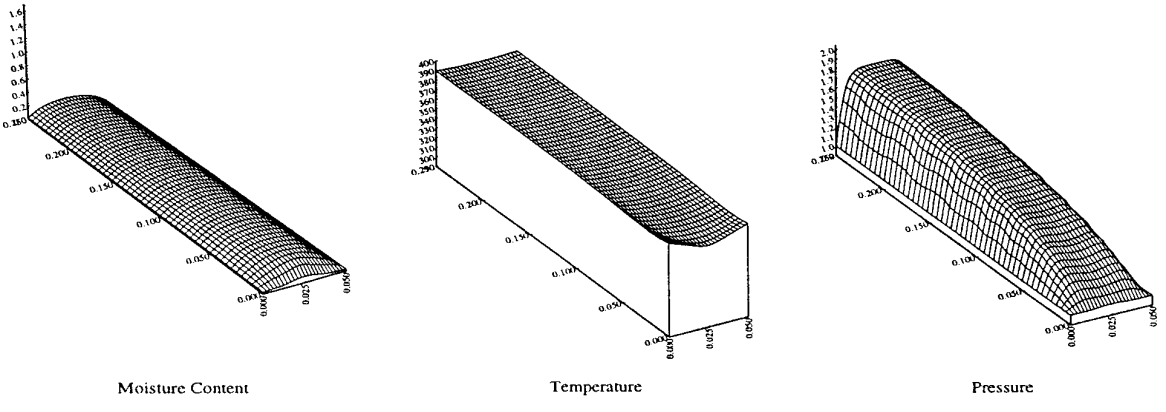

FIG. 15. Dry bulb, 120; wet bulb, 80; time, 25 h.

Figures 8, 9, and 10 show the three-dimensional surface plots of the moisture content, temperature, and pressure calculated by the control volume finite element computational model at 10, 25, and 50 h. A characteristic of low temperature timber drying is the development of an under-pressure. This can be seen in Figs. 8 to 10. The under-pressure, or *partial vacuum* effect, is caused by the temperature gradient driving moisture, in liquid form, through the pores of the body towards the surface. The volume of the voids increases causing an under-pressure to develop, which, in turn, inhibits the movement of moisture within the timber. This example exhibits an under-pressure within the centre of the timber together with an over-pressure near the exchange surfaces.

5.2. *Case* 2: *Dry bulb*, 120°C; *Wet bulb*, 80°C

The second drying problem to be presented concerns a timber sample in a high temperature airstream, having a wet bulb temperature of 80°C and a dry bulb temperature of 120°C. Figures 11 to 15 show the three-dimensional surface plots of the moisture content, temperature, and pressure calculated by the control volume finite element computational model at 5, 10, 15, 20, and 25 h. It should be noted that for this drying example, the dry bulb temperature of the airstream is above the boiling point of water. The high temperatures which occur within the interior of the timber cause a rapid internal vaporization to take place, which in turn causes an increase in the pressure within the voids of the porous material. The over-pressure can be quite clearly seen in Figs. 11 to 15 and is a characteristic of high temperature timber drying.

The over-pressure forces moisture, both in the liquid and gaseous phases, from the interior of the timber sample towards the surfaces. Timber is highly anisotropic with the difference in the permeabilities due to the presence of lumens lying parallel to the longitudinal axis [24]. Due to the strongly anisotropic nature of timber, the moisture content migrates along the longitudinal direction, the most permeable direction, towards the endpiece, where it evaporates into the surrounding airstream. However, the rate at which moisture is migrating in the longitudinal direction, due to the presence of the over-pressure, is greater than the rate of evaporation at the endpiece. The results of this phenomenon is a buildup of moisture around the endpiece of the timber sample (Figs. 12 to 14). Due to the increase in moisture at the endpiece of the timber, an evaporative cooling effect keeps the temperature in that region close to the wet bulb temperature of the air. As the drying process progresses, the moisture falls to the equilibrium moisture content value, the temperature of the timber approaches the dry bulb temperature of the surrounding airstream and the over-pressure within the timber relaxes back to atmospheric pressure.

From the average moisture content versus time, Fig. 7, it appears that high temperature drying has a number of advantages over using convected air with a dry bulb temperature below the boiling point of water. In particular, it is possible to substantially reduce the overall drying times and to increase the drying rates. This implies a faster processing time which in turn would improve the throughput and efficiency of a small industrial dryer.

6. CONCLUSIONS

The results of the timber drying examples presented in this paper indicate that the *control volume finite element* method, otherwise known as the *vertex centred control volume* method, is an applicable tool to be employed in the solution of the complex and highly non-linear timber drying equations. Ferguson and Turner [16] studied the comparison of the finite element and the cell-centred control volume method applied to timber drying problems below the boiling point of water, whereas Perre and Degiovanni [22] studied low and high temperature drying of spruce. The results presented in this paper, for both the low and high temperature drying cases, exhibit the same characteristics as those obtained using a finite element or cell-centred control volume model as discussed by those authors, Fig. 7. Future work includes a more detailed comparison of the results between the differing unstructured control volume computational techniques and a study of the control volume finite element computational mesh dependencies. The control volume method has the advantage of being conservative across each control volume, as well as being able to solve the timber drying equations on an unstructured mesh, without alteration to the formulation. During the drying process the timber distorts due to stresses which develop within the timber sample. The motivation behind this research was to solve the timber drying equations, with a coupled stress analysis module, on a mesh which deforms as the drying operation proceeds. The control volume finite element method has proven to be a versatile tool that will enable the inclusion of a coupled stress analysis module into the timber drying computational model in the future.

REFERENCES

1. H. N. Rosen, "Recent Advances in the Drying of Solid Wood," *Advances in Drying,* edited by A. S. Mujumdar (Hemisphere, New York, 1987), p. 99.
2. G. Comini and R. W. Lewis, *Int. J. Numer. Methods Eng.* **19,** 1387 (1976).
3. H. R. Thomas, K. Morgan, and R. W. Lewis, *Int. J. Numer. Methods Eng.* **15,** 1381 (1980).
4. A. V. Luikov, *Heat and Mass Transfer in Capillary-Porous Bodies* (Pergamon, Oxford, 1966).
5. A. V. Luikov, *Int. J. Heat Mass Transfer* **18,** 1 (1975).

6. W. J. Ferguson, Ph.D. thesis, University of Wales, 1991 (unpublished).
7. O. Dahlblom, H. Petersson, and S. Osmarsson, ''Numerical Simulation of the Development of Deformation and Stress in Wood during Drying,'' *4th IUFRO International Wood Drying Conference, Rotorua, New Zealand, August 1994* (New Zealand Forest Research Institute, Rotorua, New Zealand, 1994), p. 165.
8. S. Felix and P. Morlier, *Holzforschung* **46**(5), (1992).
9. S. Whitaker, *Adv. Heat Transfer* **13,** 119 (1977).
10. D. Michel, M. Quintard, and J. R. Puiggali, ''Experimental and Numerical Study of Pine Wood Drying at Low Temperature, in *Drying '87,* edited by A. S. Mujumdar (Hemisphere, Washington, DC, 1987), p. 185.
11. C. Moyne and P. Perre, *Drying Technol.* **9**(5), 1135 (1991).
12. P. Perre and C. Moyne, *Drying Technol.* **9**(5), 1153 (1991).
13. P. Perre, Ph.D. thesis, L'Université Paris, 1987.
14. I. W. Turner, *Appl. Math. Modelling,* submitted.
15. S. V. Patankar, *Numerical Heat Transfer and Fluid Flow* (McGraw–Hill, New York, 1980).
16. W. J. Ferguson and I. W. Turner, ''A Comparisonn of the Control Volume and the Finite Element Solution Techniques for the Equations Governing the Drying Process,'' in *Computational Techniques and Applications: CTAC93, Camberra, Australia, July 1993* (World Scientific, Singapore, 1993), p. 230.
17. P. Chow and M. Cross, *Int. J. Numer. Methods Eng.* **35**(9), 1849 (1992).
18. P. A. Forsyth, *SIAM J. Sci. Statist. Comput.* **12**(5), 1029 (1991).
19. L. S. Fung, A. D. Hiebert, and L. X. Nghiem, *SPE Reservoir Eng.* **15,** 349 (1992).
20. B. R. Baliga and S. V. Patankar, *Numer. Heat Transfer* **6,** 245 (1983).
21. I. W. Turner and M. Ilic, *Int. Commun. Heat Mass Transfer* **17**(1), 39 (1990).
22. P. Perre and A. Degiovanni, *Int. J. Heat Mass Transfer* **33,** 2463 (1990).
23. O. C. Zienkiewicz, *The Finite Element Method* (McGraw–Hill, London, 1977).
24. J. F. Siau, *Transport Processes in Wood* (Springer-Verlag, New York, 1990).